

Dynamic interface rearrangement in LaFeO₃/*n*-SrTiO₃ heterojunctionsSteven R. Spurgeon,^{*} Peter V. Sushko, and Scott A. Chambers[†]*Physical and Computational Sciences Directorate, Pacific Northwest National Laboratory, Richland, Washington 99352, USA*

Ryan B. Comes

*Physical and Computational Sciences Directorate, Pacific Northwest National Laboratory, Richland, Washington 99352, USA**and Department of Physics, Auburn University, Auburn, Alabama 36849, USA*

(Received 23 August 2017; published 6 November 2017)

Thin-film synthesis methods that have developed over the past decades have unlocked emergent interface properties ranging from conductivity to ferroelectricity. However, our attempts to exercise precise control over interfaces are constrained by a limited understanding of growth pathways and kinetics. Here we demonstrate that shuttered molecular beam epitaxy induces rearrangements of atomic planes at a polar/nonpolar junction of LaFeO₃ (LFO)/*n*-SrTiO₃ (STO) depending on the substrate termination. Surface characterization confirms that substrates with two different (TiO₂ and SrO) terminations were prepared prior to LFO deposition; however, local electron-energy-loss spectroscopy measurements of the final heterojunctions show a predominantly LaO/TiO₂ interfacial junction in both cases. *Ab initio* simulations suggest that the interfaces can be stabilized by trapping extra oxygen (in LaO/TiO₂) and forming oxygen vacancies (in FeO₂/SrO), which points to different growth kinetics in each case and may explain the apparent disappearance of the FeO₂/SrO interface. We conclude that judicious control of deposition time scales can be used to modify growth pathways, opening new avenues to control the structure and properties of interfacial systems.

DOI: [10.1103/PhysRevMaterials.1.063401](https://doi.org/10.1103/PhysRevMaterials.1.063401)**I. INTRODUCTION**

The predictive design and synthesis of robust functional interfaces represents the next frontier for oxide materials. While many model systems have been explored theoretically and experimentally, it is increasingly apparent that an insufficient understanding of growth pathways poses a roadblock to achieving predicted properties in real systems. Previous studies have identified several defect factors that affect the structure of oxide interfaces, including misfit strain [1], oxygen vacancies [2], cation intermixing [3], and the migration of entire lattice planes [4]. This last mechanism has been called “dynamic layer rearrangement” by Lee *et al.*, who found that it is energetically favorable for SrO ↔ TiO₂ planar swapping to occur during the synthesis of (AO)(BO₃)_{*n*} Ruddlesden-Popper phases [4,5]; their analysis prompted the use of a floating SrO surface layer to stabilize the incorporation of rocksalt SrO into the desired Sr₂TiO₄ phase. Saint-Girons *et al.* also invoked a SrO ↔ TiO₂ rearrangement mechanism to explain the coalescence of SrTiO₃ (STO) islands grown on Si, which they termed a “knitting machine” process [6]. These studies show how the mobility of lattice planes during nonequilibrium growth processes can introduce significant, potentially useful, deviations from an ideal structure. A careful experimental investigation of the evolution of the near-surface region, in conjunction with growth pathway modeling, may offer unique insight into the stability and synthesis of oxide heterojunctions.

Oxide molecular beam epitaxy (MBE), with its ability to produce single-crystalline thin films a monolayer at a time [7,8], represents the ideal method to explore the dynamic rearrangement process. In contrast to the coevaporative nature of other techniques, such as pulsed laser deposition (PLD),

MBE permits shuttering of elemental sources, which provides an additional degree of freedom to control stoichiometry and layer configurations. Layer-by-layer deposition of films and heterostructures offers the unique opportunity to harness kinetic controls by untangling processes that occur under conditions far from equilibrium. Here we consider the application of the shuttered growth mode to the synthesis of polar/nonpolar LaFeO₃ (LFO)/*n*-STO interfaces, which have been shown to possess a suitable band gap and built-in potential for photochemical water splitting [9–11]. Nakamura *et al.* reported properties of LFO grown on SrO- and TiO₂-terminated bulk STO substrates using PLD [12]; the authors observed different film polarization states in the heterojunctions, which they attributed to differing local dipole magnitudes. A subsequent photoconductivity study [13] of PLD-grown LFO/STO heterojunctions by Nakamura *et al.* also proposed the existence of different interface charge states. Comes and Chambers evaluated the effect of substrate termination directly [10]. Toward that end, they analyzed the electronic structure of LFO grown on SrO- and TiO₂-terminated STO layers using shuttered MBE growth; while the authors confirmed the appropriate terminations using angle-resolved x-ray photoelectron spectroscopy (AR-XPS), they observed a negligible impact on the potential gradient across the heterojunction. These conflicting results call for further investigation into the LFO growth mechanisms that influence the properties of the heterojunction.

We use a combination of aberration-corrected scanning transmission electron microscopy (STEM) and *ab initio* simulations to probe the atomic-scale configuration of the LFO/*n*-STO interface. Electron-energy-loss spectroscopy (STEM-EELS) measurements reveal interfaces with no planar defects that appear to have LaO/TiO₂ compositions in both cases, in contrast to the clear differences between TiO₂ and SrO terminations confirmed by AR-XPS prior to LFO deposition [10]. Fine-structure measurements show no evidence for

^{*}steven.spurgeon@pnnl.gov[†]sa.chambers@pnnl.gov

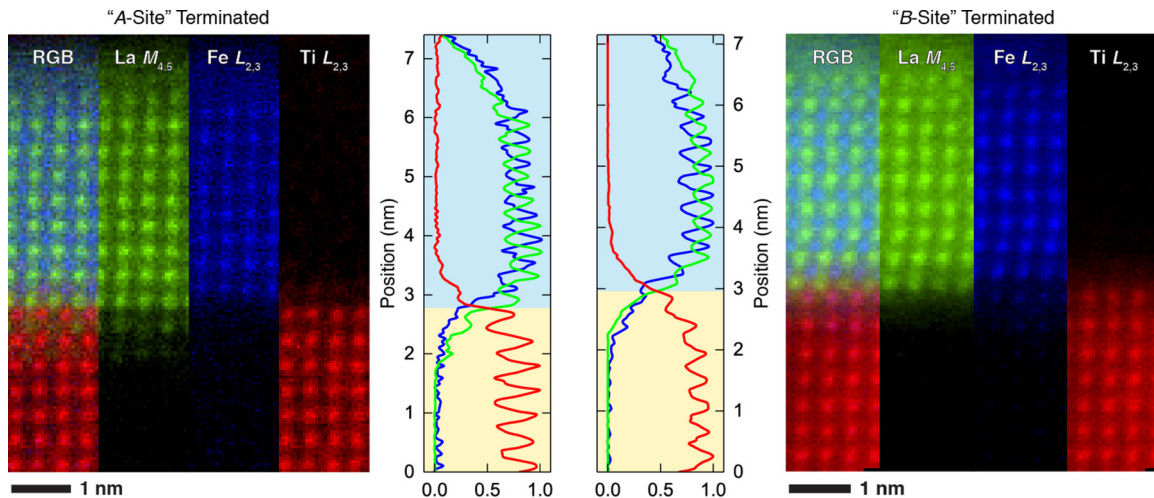


FIG. 1. Cross-sectional STEM-EELS mapping of local composition. PCA-filtered composite, La $M_{4,5}$, Fe $L_{2,3}$, and Ti $L_{2,3}$ integrated signal maps, alongside the integrated line profiles for the nominal “A-terminated” (left) and “B-terminated” (right) samples, respectively. The shaded regions mark the film-substrate interface.

oxygen vacancies, but we do observe some Fe valence changes at the interface. To interpret these results, we conduct *ab initio* simulations of the initial stages of LFO adsorption onto STO, which suggest that FeO_2/SrO is highly unstable and can transform into a LaO/TiO_2 interface. Swapping of the surface plane during film deposition can replace the terminal STO plane, pushing the system toward a LaO/TiO_2 -like interface configuration for both cases. This mechanism may partially erase the different potential gradients between the samples, explaining the discrepancy among previous reports of the interface electronic structure. Our results illustrate how the surface stability of alloying elements can give rise to unexpected heterojunction configurations. We advocate a rational design approach that considers the thermodynamic and kinetic factors associated with different substrate terminations to achieve specific synthesis outcomes.

II. METHODS

We have prepared LFO/*n*-STO (001) heterojunctions using oxygen-assisted MBE, as described elsewhere [10]. Several 0.05% Nb-doped STO substrates were chemically treated to achieve a TiO_2 substrate termination, which we confirmed using AR-XPS. A single SrO layer was then deposited on a subset of the samples, and the resulting termination was also confirmed via AR-XPS. Finally, LFO was deposited in a shuttered growth sequence with the FeO_2 (LaO) layer deposited on SrO (TiO_2), respectively. Here we discuss the nine unit cell (u.c.)-thick films; we call the FeO_2/SrO configuration the “A-terminated” sample and the LaO/TiO_2 configuration the “B-terminated” sample. Details of the synthesis and characterization procedures are given in Ref. [10].

Cross-sectional STEM samples were prepared using an FEI Helios NanoLab Dual-Beam Focused Ion Beam (FIB) microscope and a standard lift out procedure along the STO [100] zone axis, with initial cuts made at $30 \text{ kV}/2^\circ$ and final polishing at $1 \text{ kV}/3^\circ$ incidence angles. High-angle annular dark field (STEM-HAADF) images and STEM-EELS maps were collected on a JEOL ARM-200CF microscope operating

at 200 kV, with a convergence semiangle of 27.5 mrad and an STEM-EELS collection angle of 42.9 mrad. STEM-EELS maps were collected using an $\sim 1 \text{ \AA}$ probe size with an $\sim 130 \text{ pA}$ probe current and a 0.25 eV ch^{-1} dispersion, yielding an effective energy resolution of 0.75 eV. The composition maps shown in the supplemental material [14] were acquired with a 1 eV ch^{-1} dispersion and a $4\times$ energy binning. No plural scattering correction was performed, since zero loss measurements confirm that the samples are sufficiently thin ($t/\lambda < 0.76$ inelastic mean free paths). The resulting spectrum images were processed to remove x-ray spikes, and principal component analysis (PCA) was used to enhance the signal-to-noise ratio of the composition maps in Fig. 1. Figure 2 shows the raw, power-law background spectra extracted from each unit cell of the map.

$\text{LaFeO}_3/\text{SrTiO}_3$ interfaces were represented using the periodic slab model, where the LaFeO_3 and SrTiO_3 parts were each 4 u.c. thick. The 2×2 lateral cell with the in-plane lattice parameter corresponding to bulk STO ($a = b = 3.905 \text{ \AA}$) was used. The supercell parameter along the c axis was 50 \AA , which leaves a vacuum gap of over 20 \AA . The total energy of the system was minimized with respect to all degrees of freedom of the slab, unless stated otherwise. The calculations were performed using the Vienna *Ab Initio* Simulation Package [15,16]. The projected augmented wave method was used to approximate the electron-ion potential [17]. Exchange-correlation effects were treated within the Perdew-Burke-Ernzerhof (PBE) functional form, modified for solids [18]. The plane-wave basis with a 500 eV cutoff and the $2 \times 2 \times 1$ Monkhorst-Pack k -point mesh were used. The charge- and spin-density distributions were analyzed using the Bader method [19,20]. The energies of self-consistent calculations were converged to a 10^{-5} eV/cell , and the convergence of the total energy with respect to atomic coordinates was 10^{-4} eV .

III. RESULTS AND DISCUSSION

Figure 1 shows representative STEM-EELS composition maps for the nominally “A-terminated” and “B-terminated”

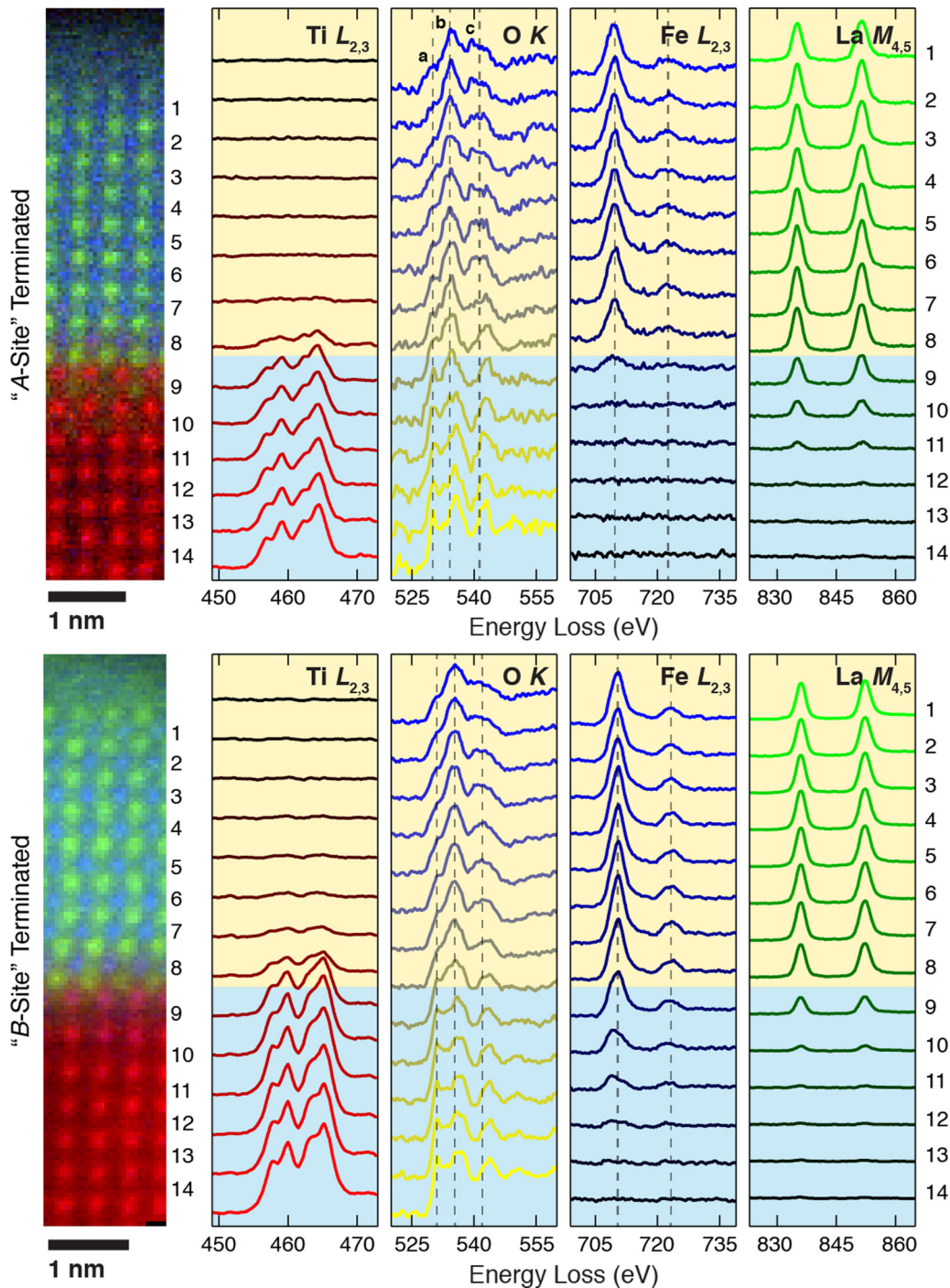


FIG. 2. Cross-sectional STEM-EELS mapping of local chemistry. PCA-filtered composition map and spectra for the $\text{Ti } L_{2,3}$, $\text{O } K$, $\text{Fe } L_{2,3}$, and $\text{La } M_{4,5}$ edges extracted from the unit cells labeled 1–14 for the nominal “A-terminated” (top) and “B-terminated” (bottom) samples, respectively. The shaded regions indicate the film-substrate interface, and the dashed lines have been added as guides to the eye. The spectra have been treated to remove x-ray spikes and the power-law background has been subtracted, but they are otherwise not denoised.

substrates. The most obvious feature is the similarity of the maps; in particular, both junctions have the same LaO/TiO_2 structure. This observation contrasts with the clear difference between the substrates prior to film deposition, as determined using AR-XPS and reflection high-energy electron diffraction (RHEED) [10]. The integrated line profiles averaged in the plane of the film confirm a $\text{FeO}_2/\text{LaO}/\text{TiO}_2/\text{SrO}$ interface stacking sequence for both samples, a finding consistent across

multiple film regions and further confirmed in the Sr maps presented in Fig. S1 of the supplemental material [14]. For the “A-terminated” sample, we find that Ti drops off to a negligible level just 1 u.c. into the LFO, while it extends 2 u.c. for the “B-terminated” sample. Similarly, we find that the Fe signal extends just 1 u.c. into the STO for the “A-terminated” sample, while it penetrates 3 u.c. for the “B-terminated” sample. It is possible that Fe_{Ti} substitution could

introduce some free carriers into the system [21]. However, previous investigations of $\text{LaCrO}_3/\text{STO}$ superlattices have shown that similar Cr_{Ti} substitutions have a minimal effect on the electrostatic potential [22,23], a finding in line with our AR-XPS measurements of these samples [10]. Conversely, the La signal extends 3 u.c. into the STO for the “A-terminated” sample and only 2 u.c. for the “B-terminated” sample. These results are also consistent with increased Sr intermixing for the “A-terminated” sample, as shown in Fig. S1 of the supplemental material [14]. La_{Sr} substitution could lead to electron doping of the STO, affecting the local electric field, but the low level of intermixing is unlikely to account for the dramatic change in the terminal STO layer.

We next investigate spectral features in the EELS fine structure that would indicate chemical state changes and may point to a mechanism for interfacial reconstruction. Figure 2 shows the Ti $L_{2,3}$, O K , Fe $L_{2,3}$, and La $M_{4,5}$ edges extracted from each u.c. across the interface for the nominally “A-terminated” and “B-terminated” substrates, respectively. We find that the Ti $L_{2,3}$ edge line shape is preserved from the STO bulk all the way up to the interface, within the 0.75 eV effective absolute energy resolution of our map. We observe no change in the Ti t_{2g} and e_g peaks that would indicate a transition from Ti^{4+} to Ti^{3+} valence states [24].

The O K edge is highly sensitive to local bonding in perovskite oxides [25], with the distribution of spectral features acting as a guide to local chemical states. Inspection of Fig. 2 reveals three distinct edge features (labeled **a–c**), resulting from the hybridization of O $2p$ states with B -site $3d$, La $5d$, and B -site $4sp$ bands, respectively [25]. We find that the pre- to main-peak (**a/b**) ratio, a known indicator of valence changes, remains largely constant on the LFO side for both terminations; similarly, there is no broadening of the main peak **b** that would indicate the formation of oxygen vacancies at the interface [26]. On the STO side, we do observe a small decrease in the **a/b** ratio moving from the bulk to within 2 u.c. of the interface for the “B-terminated” sample, suggesting some B -site valence modification; similar behavior is present in the (slightly noisier) spectra for the “A-terminated” sample.

Turning to the Fe $L_{2,3}$ edge, we first note that the edge position remains unchanged throughout the LFO for both substrate terminations. However, we observe a measurable Fe signal 1 u.c. into the STO (spectrum 9) for the “A-terminated” sample and a Fe signal 3 u.c. into the STO (spectrum 11) for the “B-terminated” sample. In the latter sample, we measure a 1.75 eV shift of the Fe L_3 edge to lower energy loss beginning at spectrum 10, which indicates a slight reduction in the Fe valence toward a more Fe^{2+} -like state [27]. This trend is clearly shown in Fig. S2 of the supplemental material [14], where it is compared to reference spectra taken from the literature. To the best of our knowledge, electron transfer to the Fe ions in this system has not been previously observed, but this behavior agrees well with changes present in the O K edge spectra, as well as predictions of interface conductivity [28]. Unfortunately, we are unable to perform transport measurements to directly measure conductivity due to the conductive Nb-STO substrate. Finally, although we do not detect any significant changes in the La $M_{4,5}$ edge line shape, we do find that its signal penetrates 1 u.c. deeper in the case of the “A-terminated” sample (a finding present in multiple

maps). In summary, we observe no clear modification of the Ti valence, but features of the O K and Fe $L_{2,3}$ edge spectra support a slight reduction in the Fe valence within the top three STO u.c. for the “B-terminated” sample. While some changes in the O K edge are also present in the “A-terminated” sample, we observe no comparable shift of the Fe $L_{2,3}$ edge.

Our STEM-EELS composition maps reveal minimal intermixing with no apparent long-range diffusion that would give rise to the rearrangement of the terminal STO layer. We find no evidence for oxygen vacancies and observe only a slight Fe valence reduction, which our prior AR-XPS results show to have a negligible impact on the measured potential [10]. The reduction in the Fe valence without oxygen vacancies is to be expected for Fe^{3+} at the interface or alloyed with n -doped STO due to the propensity of Ti^{3+} ions to transfer charge to Fe^{3+} , which has been observed in $\text{LaTiO}_3/\text{LaFeO}_3$ interfaces [29] and $\text{Sr}_{1-2x}\text{La}_{2x}\text{Ti}_{1-x}\text{Fe}_x\text{O}_3$ films [30]. This transfer leads to the formation of Fe^{2+} , which is observed in the EELS data and in the previous works.

To rationalize the disappearance of the FeO_2/SrO interface, we examined the stability of LFO grown on SrO- and TiO_2 -terminated STO using *ab initio* simulations, as shown in Fig. 3. The relative stability of the FeO_2/SrO and LaO/TiO_2 interfaces was evaluated in terms of separation energies of the LFO and STO slabs. We found that the FeO_2/SrO interface is 0.86 eV per 1×1 lateral cell, and is less stable than LaO/TiO_2 . A similar energy difference (0.8 eV per cell) was obtained by calculating the energy gain from depositing 1 u.c. of LFO on 5 u.c. thick TiO_2 -terminated slabs of STO versus on 5.5 u.c. thick SrO-terminated slabs of STO. The lower stability of the FeO_2/SrO interface is consistent with its apparent absence in the case of LFO grown on SrO-terminated STO (cf. Fig. 1).

Examination of the middle and right panels of Fig. 3 shows that FeO_2/SrO can transform into a LaO/TiO_2 interface if either Fe or Sr at this interface is replaced with Ti or La, respectively. To assess the likelihood of such transformations, we considered several configurations that correspond to Ti-Fe intermixing so that between 50% and 75% of the Fe species at the FeO_2/SrO interface are dissolved into STO. These configurations include Fe atoms arranged in the column and screw with 25% site occupancy and in two neighboring and next-neighboring planes with 50% site occupancy. Equivalent configurations were considered for Sr dissolved over La sites in the LFO part of the slab. Our calculations suggest that, in the case of Sr, such intermixing results in an energy gain of up to 0.5 eV per 2×2 cell, while equivalent Fe-Ti intermixing configurations correspond to an energy cost over 1 eV. This trend is consistent with previous reports on Ti-Al intermixing at the LaO/TiO_2 interface in $\text{LaAlO}_3/\text{STO}$ [3], where the opposite interface polarity mismatch is compensated by intermixing of the B -site species.

While intermixing is present for both FeO_2/SrO and LaO/TiO_2 interfaces, its effect on interface structure is more pronounced in the former. Here we consider the initial stages of the LFO growth to understand the origin of this asymmetry. Since MBE deposition of LFO was performed in the shuttered growth mode, we assume that the asymmetry in the structure of FeO_2/SrO and LaO/TiO_2 interfaces is mainly determined by sequential deposition of the first Fe- (in the case of

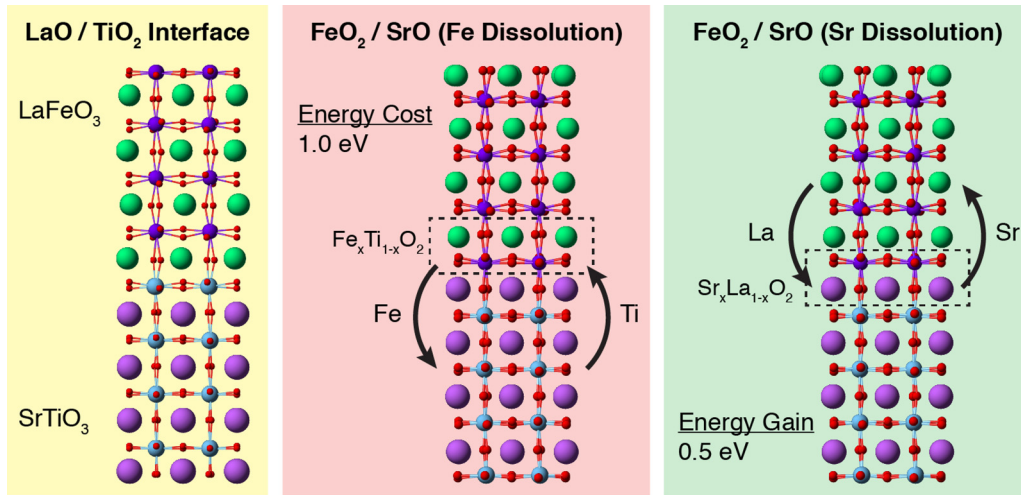


FIG. 3. Possible interface rearrangements and corresponding calculated energies. The left panel shows the stable case of the LaO/TiO₂ interface, while the middle and right panels show energetically unfavorable and favorable FeO₂/SrO interface configurations, respectively. The listed energies are calculated for the $x = 0.25$ composition. Green = La, magenta = Sr, blue = Fe, cyan = Ti, and red = O atoms.

FeO₂/SrO) and La-containing (in the case of LaO/TiO₂) planes, respectively.

Since La atoms have three valence electrons, the formation of the LaO film on TiO₂-terminated STO leaves one valence electron per La. According to our calculations, this remaining valence electron is either transferred to the STO conduction band or, in the presence of oxygen, it gets trapped by the oxygen molecules that adsorb on the LaO film in the form of negatively charged oxygen species; the calculated Gibbs free energies for the latter mechanism are shown on the left side of Fig. 4. In either case, the LaO plane as such is ordered and stoichiometric.

In contrast, the formation of an ordered stoichiometric FeO₂ plane on SrO-terminated STO is unlikely. Such a plane would

feature Fe⁴⁺ ions that are unstable in the bulk form, even under normal conditions [31]. In our case, deposition conditions result in a Fe₂O₃ composition of the plane, which corresponds to two oxygen vacancies per 2 × 2 lateral cell (see the right side of Fig. 4). While an investigation of the dynamics of such a nominally FeO₂/SrO interface is beyond the scope of the present work, it is clear that oxygen vacancies in this plane can facilitate complex rearrangements of oxygen atoms and cations that could amount to conversion of the FeO₂/SrO interface to another structure. Similar trends are obtained using the PBESOL+*U*, as shown in the supplemental material [14]. In this case, the LaO + extra-O configurations become more stable because the +*U*(Ti) correction shifts the STO conduction band to higher energies, thus promoting electron transfer to the adsorbed oxygen species. Similarly, FeO₂ configurations with oxygen vacancies become more stable because +*U*(Fe) shifts occupied Fe 3*d* states into the valence band, thus promoting charge transfer of the form Fe⁴⁺ + O²⁻ → Fe³⁺ + O⁻. This, in turn, promotes the formation of oxygen vacancies.

IV. CONCLUSIONS

Our results illustrate the dramatic effects and nonequilibrium nature of shuttered growth, as well as the importance of thermodynamic and kinetic considerations to design targeted oxide heterostructures. STEM-EELS shows that shuttered MBE growth is able to produce exceptionally high-quality and defect-free LFO/*n*-STO interfaces. However, while AR-XPS indicates that two different STO substrate terminations were achieved prior to LFO deposition, atomic-scale composition mapping of the final as-grown heterojunctions reveals a LaO/TiO₂ interface structure for both cases. We observe no long-range film-substrate cation migration and minimal valence changes, suggesting that other factors must lead to the observed structure. *Ab initio* simulations of interface stability show that FeO₂/SrO is much less energetically preferred than LaO/TiO₂. We propose that the sequential nature of the shuttered growth mode may lead to unstable Fe⁴⁺ ions that can

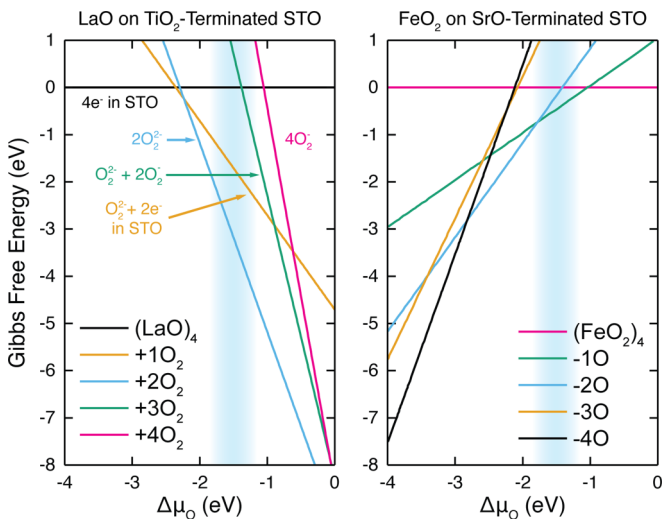


FIG. 4. Calculated Gibbs free energies for the LaO and FeO₂ planes (2 × 2 lateral cell) deposited on the TiO₂- (left) and SrO-terminated STO (right), respectively, as a function of oxygen chemical potential. Under our deposition conditions (indicated by the shaded region), the LaO film adopts an oxygen-rich configuration, while the FeO₂ plane is oxygen-deficient.

drive the system toward a dynamic structural rearrangement via oxygen vacancies. Further modeling of potential kinetic pathways and experimental study into the effects of shuttering sequence may open new ways to deterministically control the structure and properties of oxide interfaces.

ACKNOWLEDGMENTS

This work was supported by the U.S. Department of Energy, Office of Science, Division of Materials Sciences and

Engineering under Award No. 10122. Growth was supported by the Linus Pauling Distinguished Postdoctoral Fellowship at Pacific Northwest National Laboratory (PNNL LDRD PN13100/2581). All work was performed in the Environmental Molecular Sciences Laboratory, a national science user facility sponsored by the Department of Energy's Office of Biological and Environmental Research and located at Pacific Northwest National Laboratory. Pacific Northwest National Laboratory (PNNL) is a multiprogram national laboratory operated for DOE by Battelle.

-
- [1] P. S. S. R. Krishnan, A. N. Morozovska, E. A. Eliseev, Q. M. Ramasse, D. Kepaptsoglou, W.-I. Liang, Y.-H. Chu, P. Munroe, and V. Nagarajan, *J. Appl. Phys.* **115**, 054103 (2014).
- [2] N. Nakagawa, H. Y. Hwang, and D. A. Muller, *Nat. Mater.* **5**, 204 (2006).
- [3] S. Chambers, M. Engelhard, V. Shutthanandan, Z. Zhu, T. Droubay, L. Qiao, P. Sushko, T. Feng, H. Lee, T. Gustafsson, E. Garfunkel, A. Shah, J.-M. Zuo, and Q. Ramasse, *Surf. Sci. Rep.* **65**, 317 (2010).
- [4] J. H. Lee, G. Luo, I. C. Tung, S. H. Chang, Z. Luo, M. Malshe, M. Gadre, A. Bhattacharya, S. M. Nakhmanson, J. A. Eastman, H. Hong, J. Jellinek, D. Morgan, D. D. Fong, and J. W. Freeland, *Nat. Mater.* **13**, 879 (2014).
- [5] Y. F. Nie, Y. Zhu, C.-H. Lee, L. F. Kourkoutis, J. A. Mundy, J. Junquera, P. Ghosez, D. J. Baek, S. Sung, X. X. Xi, K. M. Shen, D. A. Muller, and D. G. Schlom, *Nat. Commun.* **5**, 4530 (2014).
- [6] G. Saint-Girons, R. Bachelet, R. Moalla, B. Meunier, L. Louahadj, B. Canut, A. Carretero-Genevri er, J. Gazquez, P. Regreny, C. Botella, J. Penuelas, M. G. Silly, F. Sirotti, and G. Grenet, *Chem. Mater.* **28**, 5347 (2016).
- [7] S. A. Chambers, *Surf. Sci. Rep.* **39**, 105 (2000).
- [8] S. A. Chambers, *Adv. Mater.* **22**, 219 (2010).
- [9] K. A. Stoerzinger, R. Comes, S. R. Spurgeon, S. Thevuthasan, K. Ihm, E. J. Crumlin, and S. A. Chambers, *J. Phys. Chem. Lett.* **8**, 1038 (2017).
- [10] R. Comes and S. Chambers, *Phys. Rev. Lett.* **117**, 226802 (2016).
- [11] M. D. Scafetta, A. M. Cordi, J. M. Rondinelli, and S. J. May, *J. Phys.: Condens. Matter* **26**, 505502 (2014).
- [12] M. Nakamura, F. Kagawa, T. Tanigaki, H. S. Park, T. Matsuda, D. Shindo, Y. Tokura, and M. Kawasaki, *Phys. Rev. Lett.* **116**, 156801 (2016).
- [13] K. Nakamura, H. Mashiko, K. Yoshimatsu, and A. Ohtomo, *Appl. Phys. Lett.* **108**, 211605 (2016).
- [14] See Supplemental Material at <http://link.aps.org/supplemental/10.1103/PhysRevMaterials.1.063401> for additional composition maps, fine structure analysis, and details of the *ab initio* simulations.
- [15] G. Kresse and J. Furthm uller, *Phys. Rev. B* **54**, 11169 (1996).
- [16] G. Kresse and D. Joubert, *Phys. Rev. B* **59**, 1758 (1999).
- [17] P. E. Bl ochl, *Phys. Rev. B* **50**, 17953 (1994).
- [18] J. P. Perdew, A. Ruzsinszky, G. I. Csonka, O. A. Vydrov, G. E. Scuseria, L. A. Constantin, X. Zhou, and K. Burke, *Phys. Rev. Lett.* **100**, 136406 (2008).
- [19] R. Bader, *Atoms in Molecules A Quantum Theory* (Oxford University Press, Oxford, 1990).
- [20] W. Tang, E. Sanville, and G. Henkelman, *J. Phys.: Condens. Matter* **21**, 084204 (2009).
- [21] S. Steinsvik, R. Bugge, J. Gj onnes, J. Taft , and T. Norby, *J. Phys. Chem. Solids* **58**, 969 (1997).
- [22] R. B. Comes, S. R. Spurgeon, D. M. Kepaptsoglou, M. H. Engelhard, D. E. Perea, T. C. Kaspar, Q. M. Ramasse, P. V. Sushko, and S. A. Chambers, *Chem. Mater.* **29**, 1147 (2017).
- [23] R. B. Comes, S. R. Spurgeon, S. M. Heald, D. M. Kepaptsoglou, L. Jones, P. V. Ong, M. E. Bowden, Q. M. Ramasse, P. V. Sushko, and S. A. Chambers, *Adv. Mater. Interf.* **3**, 1500779 (2016).
- [24] A. Mosk, D. A. Muller, N. Nakagawa, A. Ohtomo, J. L. Grazul, and H. Y. Hwang, *Nature (London)* **430**, 657 (2004).
- [25] M. Varela, M. P. Oxley, W. Luo, J. Tao, M. Watanabe, A. R. Lupini, S. T. Pantelides, and S. J. Pennycook, *Phys. Rev. B* **79**, 085117 (2009).
- [26] M. Nord, P. E. Vullum, M. Moreau, J. E. Boschker, S. M. Selbach, R. Holmestad, and T. Tybell, *Appl. Phys. Lett.* **106**, 041604 (2015).
- [27] H. Schmid and W. Mader, *Micron* **37**, 426 (2006).
- [28] P. Xu, W. Han, P. M. Rice, J. Jeong, M. G. Samant, K. Mohseni, H. L. Meyerheim, S. Ostanin, I. V. Maznichenko, I. Mertig, E. K. U. Gross, A. Ernst, and S. S. P. Parkin, *Adv. Mater.* **29**, 1604447 (2017).
- [29] J. E. Kleibeuker, Z. Zhong, H. Nishikawa, J. Gabel, A. M uller, F. Pfaff, M. Sing, K. Held, R. Claessen, G. Koster, and G. Rijnders, *Phys. Rev. Lett.* **113**, 237402 (2014).
- [30] R. B. Comes, T. C. Kaspar, S. M. Heald, M. E. Bowden, and S. A. Chambers, *J. Phys.: Condens. Matter* **28**, 035901 (2016).
- [31] H. Falc n, J. A. Barbero, J. A. Alonso, M. J. Mart inez-Lope, and J. L. G. Fierro, *Chem. Mater.* **14**, 2325 (2002).